



## Flexible freestanding Fe<sub>2</sub>O<sub>3</sub>-SnO<sub>x</sub>-carbon nanofiber composites for Li ion battery anodes



Bhavana N. Joshi<sup>a,1</sup>, Seongpil An<sup>a,1</sup>, Yong Il Kim<sup>a</sup>, Edmund P. Samuel<sup>a</sup>, Kyo Yong Song<sup>a</sup>, Il Won Seong<sup>b</sup>, Salem S. Al-Deyab<sup>c</sup>, Mark T. Swihart<sup>d</sup>, Woo Young Yoon<sup>b,\*\*</sup>, Sam S. Yoon<sup>a,\*</sup>

<sup>a</sup> School of Mechanical Engineering, Korea University, Seoul, 02841, Republic of Korea

<sup>b</sup> Department of Materials Science & Eng., Korea University, Seoul, 02841, Republic of Korea

<sup>c</sup> Petrochemicals Research Chair, Dept. of Chem., King Saud University, Riyadh, 11451, Saudi Arabia

<sup>d</sup> Dept. of Chem. & Biological Eng., University at Buffalo, The State University of New York, Buffalo, NY, 14260-4200, USA

### ARTICLE INFO

#### Article history:

Received 14 October 2016

Received in revised form

27 December 2016

Accepted 6 January 2017

Available online 7 January 2017

#### Keywords:

Carbon nanofiber

Fe<sub>2</sub>O<sub>3</sub>

SnO<sub>x</sub>

Electrospinning

Freestanding

Lithium ion battery

### ABSTRACT

We demonstrate electrospun ternary Fe<sub>2</sub>O<sub>3</sub>-SnO<sub>x</sub>-carbon nanofiber (CNF) composites as high-performance, flexible, and freestanding anodes for Li ion batteries (LIBs). In the ternary composites, the CNF matrix accommodates volume changes of Fe and Sn during lithiation and delithiation, while also providing short Li ion diffusion pathways, which ultimately enhances the capacity of the LIB. The concentrations of Fe and Sn were varied to find the optimal composition. Higher Sn content increased capacity at slow discharge rates, but decreased capacity at higher discharge rates. Increasing Fe to Sn ratio improved performance at high discharge rates. The Fe<sub>2</sub>O<sub>3</sub>-SnO<sub>x</sub>-CNF composite fabricated at a Fe:Sn weight ratio of 3:1 exhibited a reversible capacity value of 756 mAh·g<sup>-1</sup> after 55 cycles. The materials and methods demonstrated here are unique in producing a flexible, free-standing mat with high gravimetric capacity using a simple and scalable production process.

© 2017 Elsevier B.V. All rights reserved.

### 1. Introduction

Traditionally, graphite is used as the anode material in Li ion batteries (LIBs). Graphite has a relatively low theoretical capacity of 372 mAh·g<sup>-1</sup>; composites of metal oxides and carbon can produce much higher-capacity anodes [1]. Metal oxides such as Fe<sub>2</sub>O<sub>3</sub>, NiO, Cu<sub>2</sub>O, and SnO<sub>2</sub> are potentially promising, as they are known for their abundance, low cost, and non-toxicity [2,3]. However, capacity fading and poor performance at high current densities due to dramatic volume changes during Li insertion and extraction limit the application of such metal oxide composites. Hence, composites of mixed oxides, such as Fe<sub>2</sub>O<sub>3</sub>-SnO<sub>2</sub>, TiO<sub>2</sub>-Fe<sub>2</sub>O<sub>3</sub>, and SnO<sub>2</sub>-ZnO, have been investigated and reported to show superior and more stable capacity [4,5].

Among the previously mentioned mixed oxides, Fe<sub>2</sub>O<sub>3</sub>-SnO<sub>2</sub> has been reported to show high capacity and good rate capability. The two metal oxide phases react with Li at different potentials; thus, volume expansion and contraction occur in two stages, ultimately reducing the strain and improving the stability [6]. Recently Muller et al. [7] reported on carbon-coated, Fe-doped SnO<sub>2</sub> nanoparticles. The nanoparticles were synthesized by a solution method and the carbon coating was achieved using a sucrose solution, followed by drying under air and annealing at 500 °C in an Ar atmosphere for 4 h. The electrode was fabricated in the traditional manner, with a binder and Cu foil. Zhou et al. [8] reported on Fe<sub>2</sub>O<sub>3</sub>/SnO<sub>2</sub> nano-heterostructures synthesized on a stainless steel substrate, using a combination of hydrothermal and vapor transport deposition techniques. Yan et al. [9] reported on SnO<sub>2</sub>/Fe<sub>2</sub>O<sub>3</sub> nanocubes formed by a solvothermal method; an electrode was created on Cu foil using a binder-containing slurry. Palaparty et al. mixed carbon black with SnO<sub>2</sub> particles which were coated with FeO<sub>x</sub> via ALD (atomic layer deposition) [10]. The electrode exhibited 94% capacity retention at a fairly high current rate. Wang et al. synthesized ternary Fe<sub>2</sub>O<sub>3</sub>/SnO<sub>2</sub>/rGO composites by a hydrothermal process, which exhibited 87.8% capacity retention at 200 cycles [11]. In

\* Corresponding author.

\*\* Corresponding author.

E-mail addresses: [wyyoon@korea.ac.kr](mailto:wyyoon@korea.ac.kr) (W.Y. Yoon), [skyoonyoon@korea.ac.kr](mailto:skyoonyoon@korea.ac.kr) (S.S. Yoon).

<sup>1</sup> These authors have contributed equally.

general, the use of a binder reduces the capacity of LIBs. Thus, efforts have been made to develop binder-free and current-collector-free electrodes. Xie et al. [12] reported Fe<sub>2</sub>O<sub>3</sub>-SnO<sub>2</sub> coaxially electrospun nanofibers (NF) prepared using polyvinylpyrrolidone (PVP) followed by calcination at 500 °C in air, which made the NF highly brittle. These brittle NFs were pulverized and mixed with polydopamine and again carbonized by Ar annealing at 500 °C to form binder-free self-supported electrodes. This showed the promise of electrospun NFs, but suffered from a production process with a relatively large number of steps. Liu et al. [4] reported Fe<sub>2</sub>O<sub>3</sub>-SnO<sub>2</sub> nanoparticle-decorated flexible graphene films fabricated by hydrothermal and vacuum filtration approaches. Guo et al. [13] fabricated a high-performance SnO<sub>2</sub>-Fe<sub>2</sub>O<sub>3</sub> carbon anode via a sol-gel route. However, the fabrication of flexible and freestanding Fe<sub>2</sub>O<sub>3</sub>-SnO<sub>x</sub>-carbon NF (CNF) composites has not been yet demonstrated. Flexible electrodes are important for use in foldable and portable devices, and the freestanding feature eliminates the current collector, which comprises at least 50% of the total weight of conventional electrodes. According to Wang et al. [14], the market for the flexible energy storage devices will grow substantially in coming years. Therefore, the need for a simple and low-cost fabrication process for flexible electronics will become even more important.

Herein, we demonstrate the synthesis of a flexible, freestanding Fe<sub>2</sub>O<sub>3</sub>-SnO<sub>x</sub>-CNF composite, and its high performance in capacity retention, which is important for long-term use. In addition to its electrochemical role, SnO<sub>x</sub> serves to reduce the agglomeration of Fe<sub>2</sub>O<sub>3</sub> during cycling. The electrochemical performance of these ternary Fe<sub>2</sub>O<sub>3</sub>-SnO<sub>x</sub>-CNF electrodes was tested and parametric studies were performed to determine the optimal fabrication conditions. This study is unique in providing a simple route to high-capacity flexible, binder-free, and free-standing electrodes, which requires just a single deposition step (by electrospinning) followed by heat treatment.

## 2. Experimental

Initially, 8 wt% polyacrylonitrile (PAN, *M<sub>w</sub>* = 150 kDa, Sigma-Aldrich) was dissolved in *N,N*-dimethylformamide (DMF, 99.8%, Sigma-Aldrich) and the mixture was stirred for 24 h at 60 °C. Iron (III) acetylacetonate ((FeAcAc), Fe(C<sub>5</sub>H<sub>7</sub>O<sub>2</sub>)<sub>3</sub>, Sigma-Aldrich) and tin (II) acetate ((SnAc), Sn(CH<sub>3</sub>CO<sub>2</sub>)<sub>2</sub>, Sigma-Aldrich) were dissolved in this PAN-DMF solution and the mixture was stirred for 24 h at 25 °C to form a homogenous solution. The total metal salt content added to the PAN solution was 4 wt%. Solutions with varying metal compositions were prepared, as shown in Table 1. Various proportions of metals were tested to determine the optimized concentrations of Fe<sub>2</sub>O<sub>3</sub> and SnO<sub>x</sub> that would maximize the synergistic effects of Fe<sub>2</sub>O<sub>3</sub>/SnO<sub>x</sub>.

The steps of NF mat synthesis are shown in Fig. 1. The NF mat was made by an electrospinning process, as discussed in our earlier reports [15]. The setup consists of a syringe, needle, grounded collector, and high-voltage power supply. The brown-colored precursor solution (Fig. 1a) was delivered from a syringe pump with an optimized flow rate of 250 μL/h that yielded a stable Taylor cone at the end of the needle. The electrospun fibers were collected on an

aluminum collector held 17 cm away from the needle (Fig. 1d), forming a yellow-colored mat. The synthesized mats were stabilized by heating in air at a heating rate of 5 °C/min, from room temperature to 280 °C, where they were held for 30 min (Fig. 1b). The stabilized mats were further annealed in a tube furnace under flowing Ar at 700 °C for 2 h (Fig. 1c). For Ar annealing, we increased the temperature from room temperature to 700 °C at a rate of 3 °C/min to carbonize the PAN NFs, which yielded flexible, freestanding black-colored carbonized Fe<sub>2</sub>O<sub>3</sub>/SnO<sub>x</sub>/CNF mats, as shown in Fig. 1e. These mats were then punched into circles 14 mm in diameter (Fig. 1f) to be used as working electrodes in the tested half-cell.

The prepared and carbonized freestanding mats, with a thickness of ~15 μm were characterized to determine their structural, morphological, chemical, and electrochemical properties. X-ray diffraction (XRD, SmartLab, Rigaku) was used to study the crystal-line structures of the mats. X-ray photoelectron spectroscopy (XPS, Theta Probe Base System, Thermo Fisher Scientific Co.) measurements were conducted to evaluate the chemical states of elements in the mats. The surface morphologies and elemental mapping of the fabricated mats were evaluated using a field emission scanning electron microscope (FE-SEM, S-5000, Hitachi, Ltd.) and a transmission electron microscope (TEM, JEM 2100F, JEOL Inc.). A confocal Raman spectrometer (NRS-3100, Jasco) was used to analyze the carbon content and amount of carbon defects in the mats.

### 2.1. Electrochemical tests

The electrochemical performance was measured in a CR2032 coin-type half-cell, in which the 14-mm-diameter carbonized freestanding binder-free NF mats were directly applied as anodes without a slurry-coating process. A metallic Li sheet was used as the reference electrode. A microporous polyethylene film (Celgard 2400; Celgard, South Korea) was used as the separator between the two electrodes. The electrolyte was 1-M LiPF<sub>6</sub> in a solvent mixture of ethylene carbonate (EC), dimethylcarbonate (DMC), and ethyl methyl carbonate (EMC) (1:1:1 by volume) (PuriEL Soulbrain, Seongnam, South Korea). Galvanostatic discharge/charge curves were measured at 25 °C using a WBCS3000 battery cyclers system (WonATech, South Korea). The cells were initially subjected to rate testing at different current densities (10 cycles each at 100 mA g<sup>-1</sup>, 200 mA g<sup>-1</sup>, 500 mA g<sup>-1</sup>, and 1000 mA g<sup>-1</sup>) followed by an additional cycle test at 100 mA g<sup>-1</sup>. In total, the number of cycles tested was 55.

## 3. Results and discussion

The XRD patterns of mats fabricated with different Fe:Sn ratios are shown in Fig. 2. The broad hump observed in the pattern of Case 1 is attributed to carbon from the CNFs. The patterns of Cases 2, 3, and 4 show relatively weak peaks at  $2\theta = 40.25^\circ$  and  $47.5^\circ$ , attributed to the (113) and (024) planes, respectively, of  $\alpha$ -Fe<sub>2</sub>O<sub>3</sub> (JCPDS No 24-0072). The small peak at  $2\theta = 29.19^\circ$  corresponds to the (220) planes of Fe<sub>3</sub>O<sub>4</sub>, confirming the presence of the magnetite phase (JCPDS No. 19-0629). The presence of the two phases is attributed to the reduction of Fe<sup>3+</sup> to Fe<sup>2+</sup> during carbonization [2]. Notably, the weak peaks indicate that the crystallinity is generally poor and the iron oxide crystallites are small. In Case 4, the Sn peaks positioned at  $2\theta = 30.6^\circ$ ,  $32.09^\circ$ ,  $43.9^\circ$ , and  $45.02^\circ$  correspond to the (200), (101), (220), and (211) orientations, respectively (marked with blue dotted lines). This suggests that the Sn phase is well crystallized at higher Sn concentrations, while the lower concentration in Case 3 yields a poorly crystallized phase. The broad peak at 25° in all cases is attributed to carbon from the carbonized PAN.

In Fig. 3, the SEM image of the Case 1 fibers shows a smooth morphology. The Case 2 surface appears roughly textured because

**Table 1**  
Precursor composition.

Case no.	FeAcAc:SnAc (wt%)
1	0:0
2	4:0
3	3:1
4	1:3

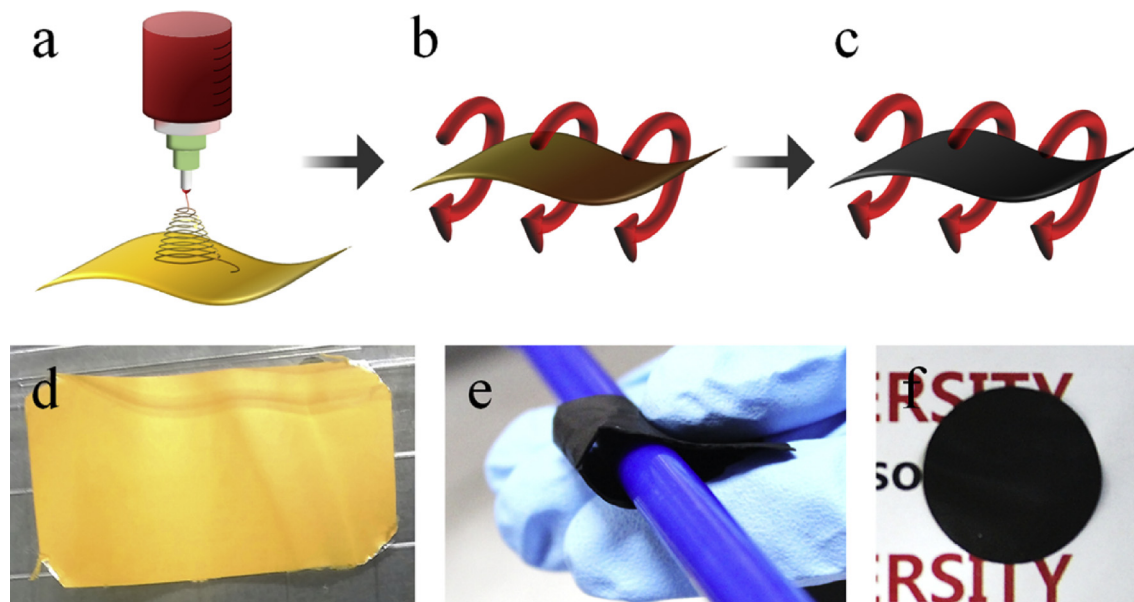


**Fig. 1.** Schematics showing steps to obtain freestanding flexible NF mat: (a) electrospinning process, (b) stabilization at 280 °C for 30 min, and (c) carbonization under Ar gas at 700 °C for 2 h. Photographs of (d) as-deposited yellow-colored mat, (e) carbonized mat with good flexibility, and (f) 14-mm-diameter circular punched mat. (For interpretation of the references to colour in this figure legend, the reader is referred to the web version of this article.)

of the  $\text{Fe}_2\text{O}_3$  formation from within the NFs. In Case 3 and Case 4, larger dots appear on the NF surfaces, which are found to be  $\text{SnO}_x$  by EDAX analysis (see Fig. S1). Sn may be driven to the surface of the fibers by stress relaxation. The difference in the thermal expansion coefficients of the component materials can create stresses that drive Sn particles outside [16]. As the Sn concentration is increased (Case 4), the dots grow larger, but appear less frequently. These Sn spheres are sporadically attached to the NF surfaces. About 100 NF samples were collected and their individual size was measured to estimate an average NF diameter for each case. The estimated fiber size is  $324 \pm 47$ ,  $252 \pm 42$ ,  $280 \pm 36$ , and  $340 \pm 38$  nm for Cases 1, 2, 3, and 4, respectively. Increasing the electrospinning precursor's electrical conductivity with greater Fe concentration reduces the diameter of a discharging jet and thus the nanofiber diameter is also reduced [17].

Raman spectra from the  $\text{Fe}_2\text{O}_3$ - $\text{SnO}_x$ -CNF composites were recorded using a 532-nm laser as the excitation source. In Fig. 4, all

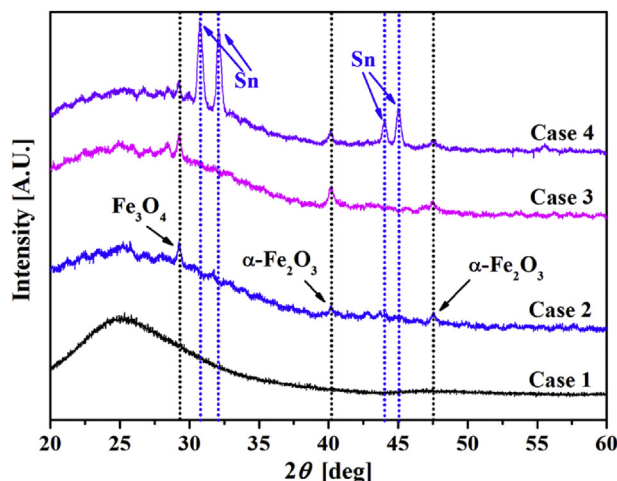


**Fig. 2.** XRD patterns of Cases 1, 2, 3, and 4.

spectra exhibit bands centered at 1350 and 1596  $\text{cm}^{-1}$ , which correspond to disordered (*D*) and graphitic (*G*) carbon, respectively, confirming carbon graphitization in all specimens. The *D*-band indicates the presence of  $\text{sp}^3$ -defects, whereas the *G*-band corresponds to the graphitic  $\text{sp}^2$ -conjugated carbon. The intensity ratio of the *D*- and *G*-bands ( $I_D/I_G$ ) for Case 1 and for the other cases (Cases 2, 3, and 4) were estimated as 1.1 and 0.78, respectively. The low  $I_D/I_G$  value ( $<1.0$ ) in Cases 2, 3, and 4 indicates improved graphitization in these composites. The lower  $I_D/I_G$  ratio indicates that the Fe precursor generates more highly ordered carbon than the pure CNF [18].

The oxidation states and elemental composition in the NF mats were determined from XPS spectra, as presented in Fig. 5. The survey spectrum is presented in Fig. S2, which shows the signals from C, N, O, Fe, and Sn. In Fig. 5a, the two peaks at ~710 eV and 725 eV, attributed to  $\text{Fe } 2p_{3/2}$  and  $\text{Fe } 2p_{1/2}$ , respectively, confirm the presence of Fe (III). The shoulder peak at ~710 eV indicates the partial reduction of  $\text{Fe}^{3+}$  to  $\text{Fe}^{2+}$ , consistent with the XRD pattern. The peaks in Fig. 5b at 486.9 eV and 495.4 eV correspond to  $\text{Sn } 3d_{5/2}$  and  $\text{Sn } 3d_{3/2}$ , respectively. The de-convoluted  $\text{Sn } 3d_{5/2}$  peak shown in Fig. S3 confirms the presence of metallic Sn, also observed in the XRD pattern. However, the  $\text{Sn}^{2+}$  and  $\text{Sn}^{4+}$  peaks only partially confirm the presence of  $\text{SnO}$  and  $\text{SnO}_2$  whereas the XPS firmly indicates the presence of  $\text{SnO}_x$  [19]. The peak at 285 eV in Fig. 5c belongs to graphitic carbon, while the shoulder at 288 eV corresponds to the C(O)O group [2]. The O 1s band is detected at 531 eV, as shown in Fig. 5d.

The distributions of  $\text{Fe}_2\text{O}_3$  and  $\text{SnO}_x$  nanoparticles were explored by high-resolution TEM (HRTEM). Fig. 6a shows a magnified view of a single  $\text{Fe}_2\text{O}_3$ - $\text{SnO}_x$ -CNF from the Case 3 mat, in which the growth of Sn nanoparticles inside the CNF is clearly visible. The inset shows the selected-area electron diffraction (SAED) pattern; all diffraction rings are indexed to tetragonal Sn. A lattice-resolved HRTEM image (Fig. 6b) of a grain observed at the edge of the NF in Fig. 6a identifies it as Sn, as confirmed from the interplanar distances of the (200) and (101) planes. Thus, TEM imaging confirms the formation of Sn nanoparticles in the  $\text{Fe}_2\text{O}_3$ - $\text{SnO}_x$ -CNF nanocomposites. Fig. 6c shows results of elemental

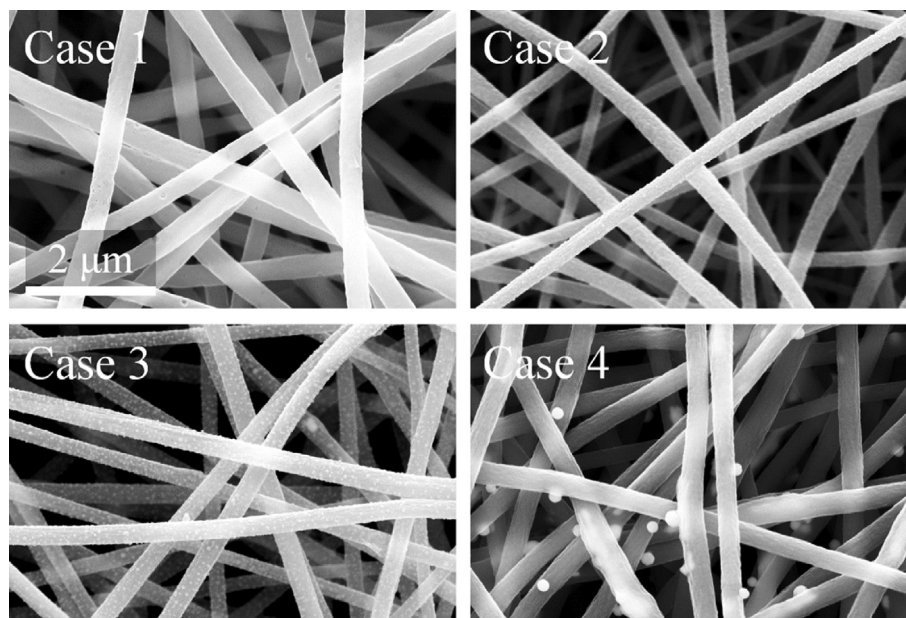
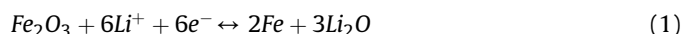


Fig. 3. SEM images of mats from Cases 1, 2, 3, and 4.

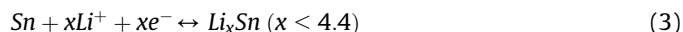
mapping, which clearly reveals the presence of C, Sn, Fe, and O distributed homogeneously along the NF. However, O is detected in low concentrations compared to that of the metal particles; see Fig. S3. Although  $\text{Fe}_2\text{O}_3$  nanoparticles are not seen in Fig. 6a, the elemental mapping confirms the presence of Fe.

Fig. 7 shows the galvanostatic charge–discharge profiles of different cycles of electrodes using Cases 1, 2, 3, and 4 composites at rate of  $100 \text{ mA g}^{-1}$ . The corresponding initial discharge/charge capacities of Cases 1, 2, 3, and 4 are  $903/677$ ,  $1030/762$ ,  $1053/797$ , and  $1458/1192 \text{ mAh} \cdot \text{g}^{-1}$  with Coulombic efficiencies of 74.9%, 73%, 75%, and 81%, respectively. The initial discharge curve shows a smooth slope in the voltage range of 2.0–0.8 V, which is attributed to the Li insertion process. A long plateau region near 0.8 V corresponds to the conversion of metal ions to metal particles [20] in Cases 2, 3, and 4. Meanwhile, in Case 1, the conductive CNF facilitates Li ion transport in the electrode, but the reversible capacity is relatively low. Irreversible capacity loss is observed in all samples in the first cycle ( $N = 1$ ), which is due to the formation of

solid electrolyte interphase (SEI) layers [1]. The specific capacity is the highest in Case 4 because it has the highest Sn concentration; the first discharge capacity of  $\text{SnO}_x$  is  $1458 \text{ mAh} \cdot \text{g}^{-1}$  [21]. The Coulombic efficiency of Case 4 reaches 81%, which is higher than that of pure  $\text{SnO}_x$ ; see Fig. S4. The high Coulombic efficiency in Case 4 is because of the relatively low  $\text{Fe}_2\text{O}_3$  content, as  $\text{Fe}_2\text{O}_3$  tends to decompose  $\text{Li}_2\text{O}$  [22]. Interestingly, in Case 3, similar reversible capacity trends are observed for  $N = 2$  and 5, implying stable capacity resulting from the mixture of  $\text{Fe}_2\text{O}_3$  and  $\text{SnO}_x$ . However, the second discharge curve is observed to differ from the first in all cases, suggesting drastic structural changes in the working electrodes due to Li insertion [20]. In the  $\text{Fe}_2\text{O}_3$ – $\text{SnO}_x$ –CNF composites, Li reacts with  $\text{Fe}_2\text{O}_3$  by a reversible conversion reaction, so that the capacity of  $\text{Fe}_2\text{O}_3$  is fully reversible, as shown below [8]:



Simultaneously,  $\text{SnO}_x$  reacts with Li in two steps, as presented in the following electrochemical reactions [23]:



The  $\text{Li}_2\text{O}$  matrix decomposition process occurs by the electrochemical formation of  $\text{Fe}^0$  and  $\text{Sn}^0$  nanoparticles, as mentioned in reactions (1) and (2). The two different types of nanoparticles in the NFs enhance the reversible capacity and increase capacity retention in the anode. The enhanced capacity of the mixed-oxide NFs may be due to the synergistic electrochemical activity of the composite electrode.

The lithiation phenomena for Cases 1–4 were analyzed further using the normalized differential capacity curves of the LIB cells, as shown in Fig. 8. In Case 1, the peaks are at 0.24 and 0.84 V during  $N = 1$ , attributed to Li insertion in the CNF and SEI formation, respectively [24]. During  $N = 2$ , the peaks almost vanish, because the SEI layer formation is completed in the first cycle. Case 2 shows peaks at 1.3 V and 0.75 V, related to the transformation of  $\text{Fe}_2\text{O}_3$  to  $\text{Fe}^0$  along with the formation of  $\text{Li}_2\text{O}$

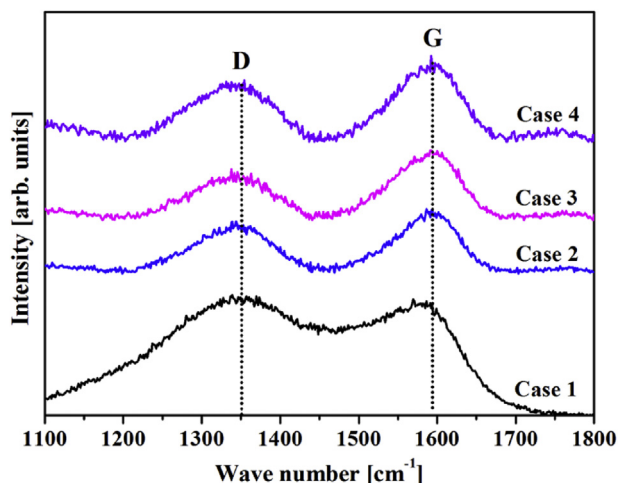


Fig. 4. Raman spectra of Case 1, 2, 3, and 4.

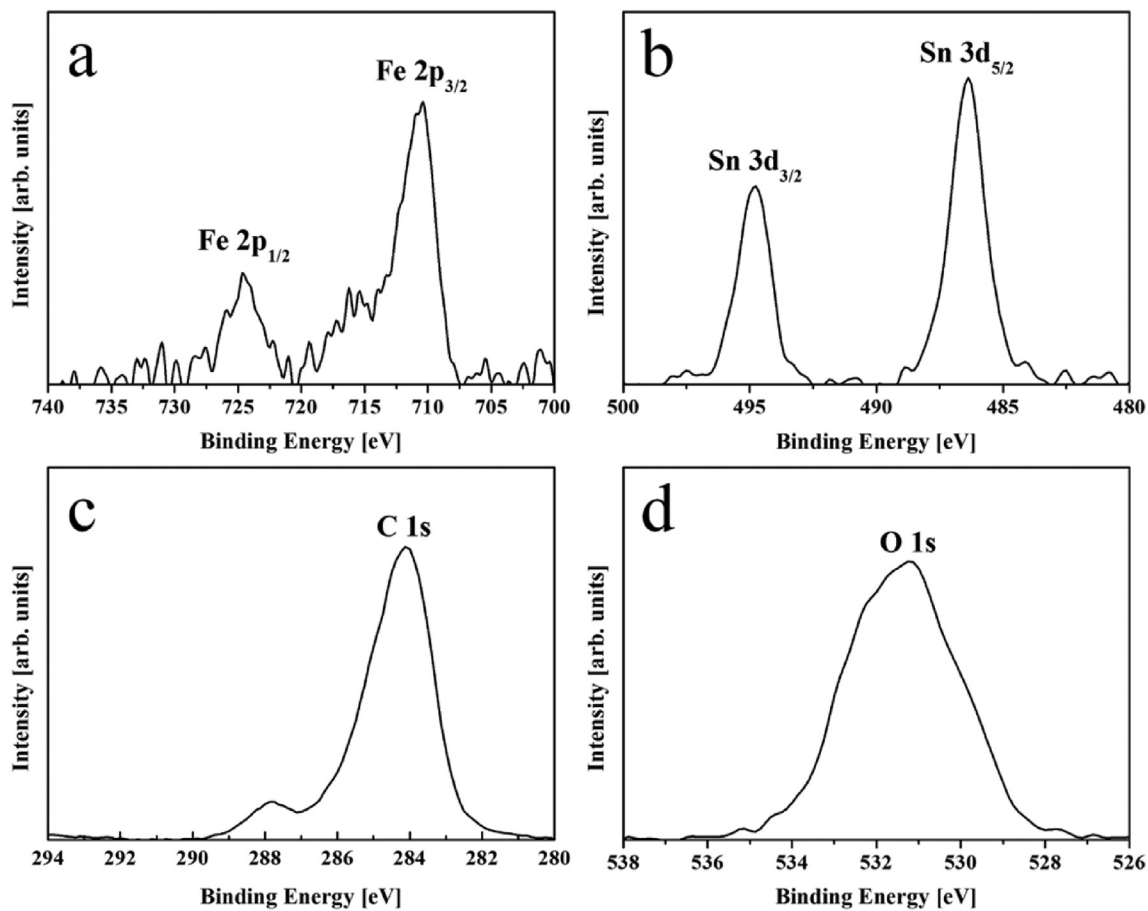


Fig. 5. High-resolution XPS spectra of Fe<sub>2</sub>O<sub>3</sub>/SnO<sub>x</sub>/CNF Case 3: (a) Fe 2p. (b) Sn 3d. (c) C 1s. (d) O 1s.

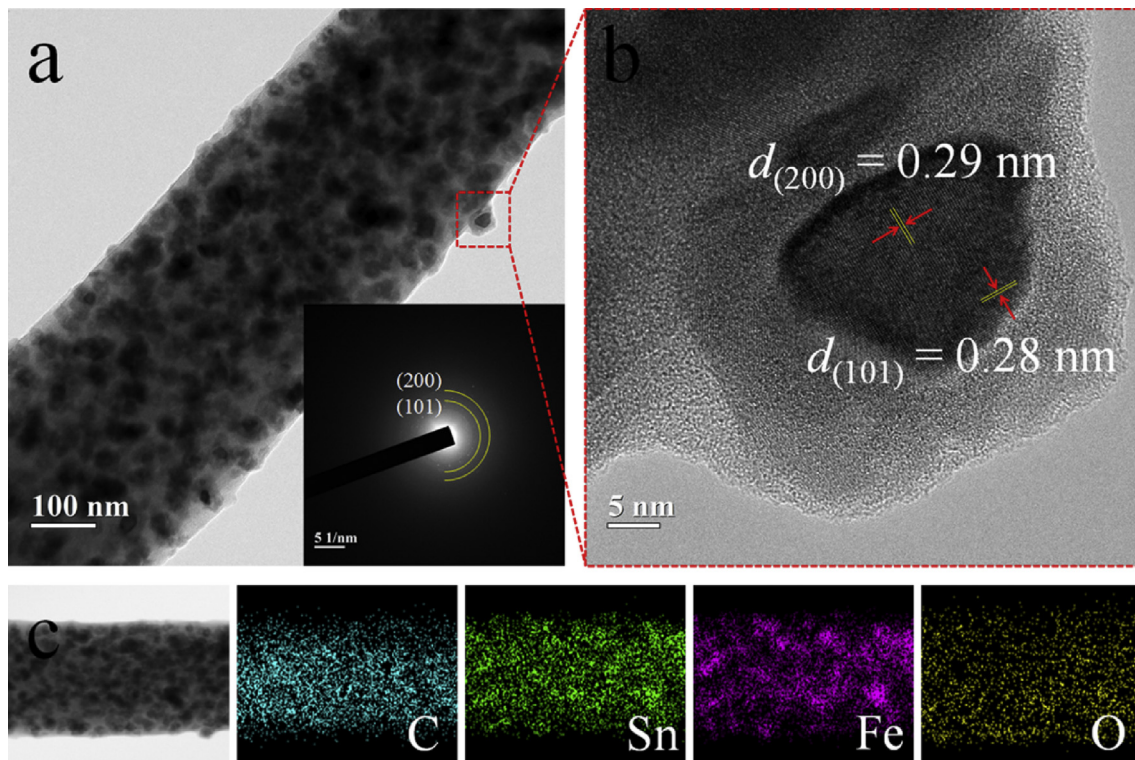


Fig. 6. TEM images of a single fiber from the Case 3 mat. (a) image with SAED pattern in the inset, (b) HRTEM image, (c) Elemental mapping of C, Sn, Fe, and O.

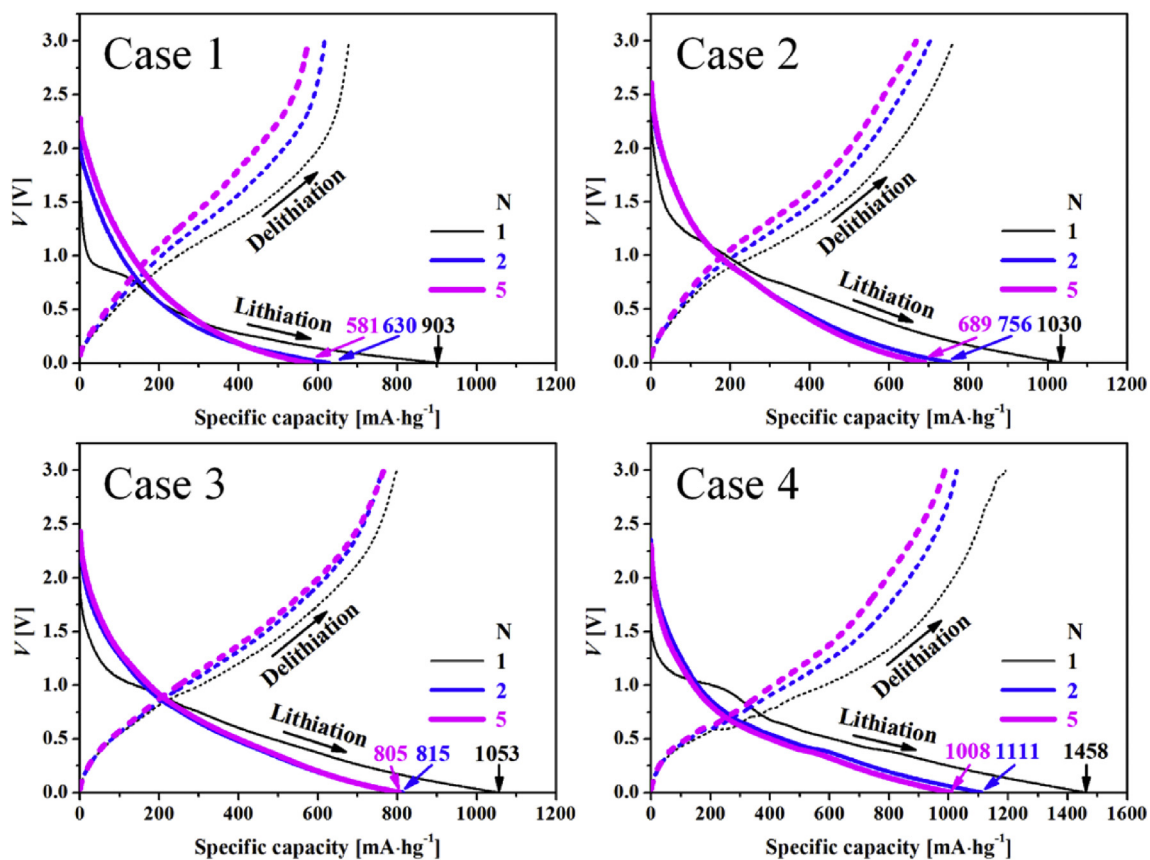
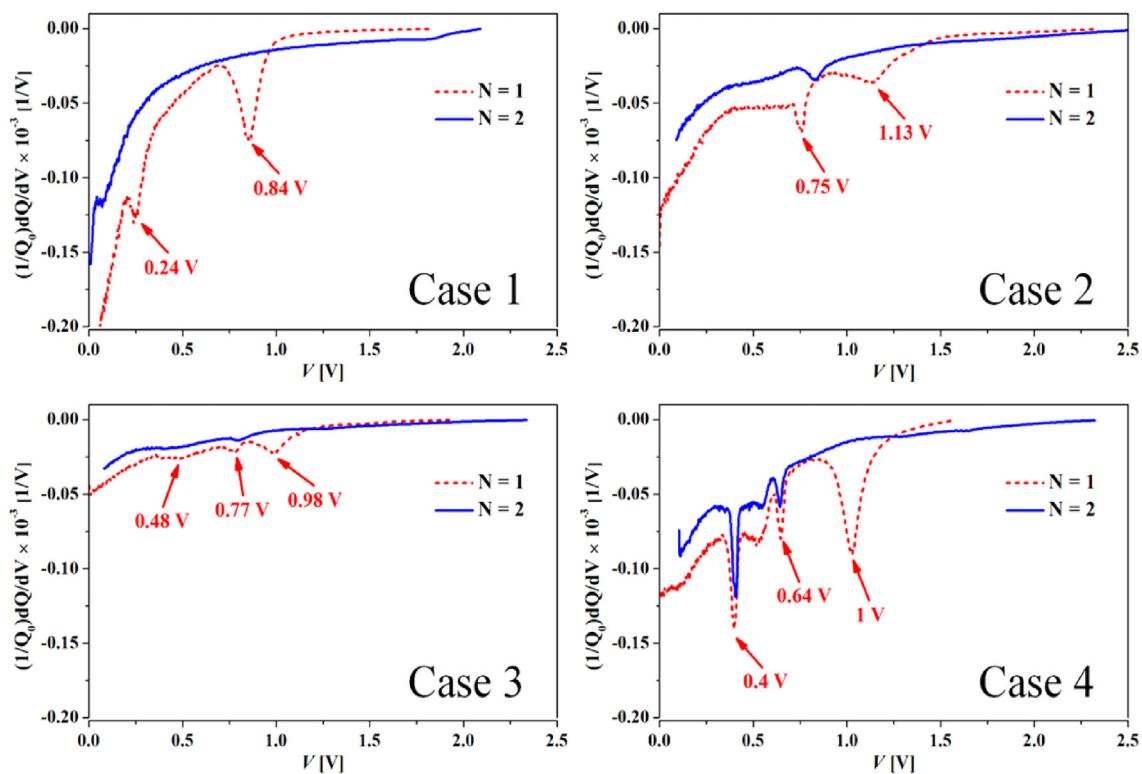
Fig. 7. Charge–discharge curves at 100 mA g<sup>-1</sup>.

Fig. 8. Differential capacity plots during lithiation of Case 1–4 electrodes.

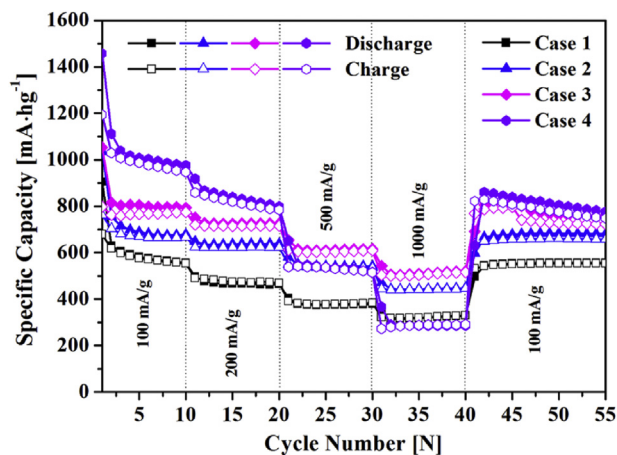


Fig. 9. Cycling performance at different current rates with voltage range of 0.001–3.0 V.

[25]. A significant impact of the composites of the two metal oxides along with CNF is observed in Cases 3 and 4. Three peaks are observed during lithiation in Case 3 at 0.98 V, 0.77 V, and 0.48 V, related to the  $\text{Fe}_2\text{O}_3$ -to- $\text{Fe}^0$ ,  $\text{Li}_2\text{O}$ , and  $\text{SnO}$ -to- $\text{Sn}$  formation reactions, respectively [25]. The shift in the  $\text{Fe}^0$  formation potential may be due to interactions of the two metal oxides in the composite. However, the appearance of two peaks related to the metal oxide-to-metal formation indicates the presence of two metal oxides together that can buffer volume changes for each other and prevent aggregation [22]. The broad and less intense peak is due to the nanoparticles embedded in the CNF. In Case 4, similar to Case 3, three peaks are observed at 1 V, 0.64 V, and 0.4 V, but the peaks are sharp and intense, possibly because of the increase in particle size with the increased concentration of Sn. This would ultimately result in greater consumption by the involvement and reaction of Li ions. However, the peak at 0.64 V is due to the formation of the  $\text{LiSn}$  alloy. Notably, in Case 4, the peaks related to alloy formation and the lithiation of Sn are observed to persist during  $N = 2$ .

The cycling performance  $\text{Fe}_2\text{O}_3$ - $\text{SnO}_x$ -CNF anodes at various currents is shown in Fig. 9. All cases show capacity decreases with increases in the current density loading. In all cases, the capacity value is restored when the current density is reset to  $100 \text{ mA g}^{-1}$ , demonstrating good rate capability for all composites. However, in Case 4, the capacity decreases significantly with increases in current rate, probably because of lithium diffusion limitations in the hundred-nanometer-size  $\text{SnO}_x$  particles positioned outside of the fibers [16]. The capacity restoration value of Case 4 remains comparable to that of Case 3 because of the presence of  $\text{Fe}_2\text{O}_3$  nanoparticles. Table 2 presents the discharge capacity values of different cases at varied current rates. Table 2 shows that addition of  $\text{Fe}_2\text{O}_3$  in pure CNF (Case 2) increases the capacity. When  $\text{SnO}_x$  is added to  $\text{Fe}_2\text{O}_3$ /CNF (Fe:Sn ~3:1) (Case 3) the capacity increased further and high capacity

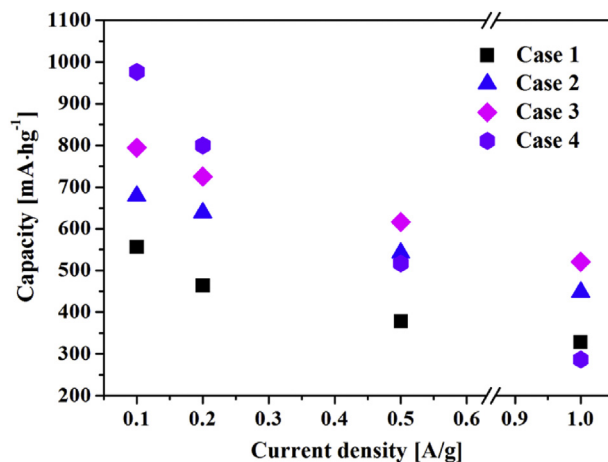


Fig. 10. Rate capability at different current rates.

was maintained at high current due to the mutual buffering effect of Fe and Sn and the small size of the metal oxide particles. Further increasing the Sn:Fe ratio produced higher capacity at low current, but gave the lowest capacity among all samples at higher current.

In summary, pure CNF cannot exhibit high-performance capacity. The inclusion of Sn boosts the capacity only at low current loading levels; at relatively high loading, the NF composites cannot maintain high capacity. The inclusion of Fe enhances the composite's performance even at relatively high current loading levels. The addition of more Sn helps to increase the performance of the ternary composite anode.

A comparative graph of the discharge capacities of all cases after each  $N = 10$  cycles at different current rates is presented in Fig. 10. The figure confirms the superior performance of the Case 3 electrode in capacity retention, as the electrode recovers its capacity to the greatest extent among all compared cases. Thus, it is clear that the Case 3 electrode can tolerate high currents; it shows a reversible capacity of  $540 \text{ mAh g}^{-1}$  at  $1 \text{ A g}^{-1}$  current density. The capacity retention in Case 3 is ~71%, exceeding previously reported values, as presented in Table 3. The reversible capacity values reported by Guo et al. [13], Liu et al. [4], and Zhao et al. [26] are significantly higher than those in the present study. However, their capacity retention (relative to the first cycle) is lower. The sol-gel film of Guo et al. and the  $\text{SnO}_2/\text{Fe}_2\text{O}_3/\text{rGO}$  particles via a hydrothermal processed by Zhao et al. were fabricated with a binder and current collector and do not provide the advantages of a flexible, free-standing film like that demonstrated here. The high gravimetric capacity, based on the mass of active material, may not be reflected in real devices where the mass of the current collector is also a factor. Although Liu et al. produced free-standing and flexible films, their method requires multiple steps, including  $\text{FeOOH}$  nanospindle synthesis, coating with  $\text{SnO}_2$  (in a 36 h process), particle collection and

Table 2  
Effect of variation of Fe/Sn on Discharge capacity at different current rate.

Case	Discharge capacity [ $\text{mAh g}^{-1}$ ]					Fe:Sn
	100 [ $\text{mA g}^{-1}$ ] N = 1	200 [ $\text{mA g}^{-1}$ ] N = 11	500 [ $\text{mA g}^{-1}$ ] N = 21	1000 [ $\text{mA g}^{-1}$ ] N = 31	100 [ $\text{mA g}^{-1}$ ] N = 41	
Case 1	903	496	403	332	497	0:0
Case 2	1034	634	580	471	596	4:0
Case 3	1053	751	654	540	692	3:1
Case 4	1458	917	651	367	631	1:3

**Table 3**  
Comparison of specific capacities reported so far with present study.

Composition	Electrode prepared	Flexibility	First discharge capacity [mAh g <sup>-1</sup> ]	First reversible capacity [mAh g <sup>-1</sup> ]	Capacity retention (Nth) [%]	Retained capacity [mAh g <sup>-1</sup> ]	Current loading [mA g <sup>-1</sup> ]	Refs.
Fe <sub>2</sub> O <sub>3</sub> /SnO <sub>2</sub> /C	Microparticles w/binder	No	1618	1131	52 (50)	841	100	[20]
Fe <sub>2</sub> O <sub>3</sub> /SnO <sub>2</sub> /C	Nanofiber w/o binder	No	1400	1075	60 (80)	840	100	[12]
Fe <sub>2</sub> O <sub>3</sub> /SnO <sub>2</sub> /SWCNT	Nanoparticle w/binder	No	1541	1000	44 (50)	680	200	[25]
			1541	1000	36 (100)	550	1000	
Fe <sub>2</sub> O <sub>3</sub> /SnO <sub>2</sub> /C	Sol-gel film w/binder	No	2605	1490	56 (150)	1460	200	[13]
Fe <sub>2</sub> O <sub>3</sub> /SnO <sub>2</sub> /Graphene	Nanoparticle w/o binder	Yes	1050	946	51 (90)	540	100	[27]
Fe <sub>2</sub> O <sub>3</sub> /SnO <sub>2</sub> /Graphene	Nanoparticle w/o binder	Yes	2063	1255	49 (200)	1010	100	[4]
Fe <sub>2</sub> O <sub>3</sub> /SnO <sub>2</sub> /graphene	Nanoparticle w/ binder	No	2150	1010	53 (100)	830	200	[26]
<b>Fe<sub>2</sub>O<sub>3</sub>/SnO<sub>x</sub>/CNF</b>	<b>Nanofibers w/o binder</b>	<b>Yes</b>	<b>1053</b>	<b>797</b>	<b>71 (55)</b>	<b>756</b>	<b>100</b>	<b>Present work</b>

Bold indicates paper's finding.

purification, mixing with separately-prepared graphene, film formation by vacuum filtration, drying, and heat treatment for electrode fabrication. By comparison, our method is simple, with one deposition step, followed by heat treatment, and *in situ* formation of the metal oxide nanoparticles. Thus, our process that uses simple processing to produce a flexible, free-standing anode with a retained capacity that is double the theoretical capacity of a graphite electrode may be of substantial practical value even though it does not match the highest performing iron-tin-carbon based anodes in the literature.

#### 4. Conclusion

In summary, we have synthesized a flexible and freestanding Fe<sub>2</sub>O<sub>3</sub>-SnO<sub>x</sub>-CNF ternary composite electrode by a simple electrospinning and carbonization processes with *in situ* formation of the metal oxide nanoparticles. The electrode with a 3:1 Fe:Sn mass ratio exhibited a high Li storage capacity at a high current (540 mAh·g<sup>-1</sup> @ 1A·g<sup>-1</sup>), 71% capacity retention (relative to the first cycle), and excellent cycling performance. The superior electrochemical properties of this electrode can be attributed to the well-embedded nanoparticles of Fe<sub>2</sub>O<sub>3</sub> and SnO<sub>x</sub> in the CNF matrix, which provides good electron transport, short Li<sup>+</sup> diffusion lengths, and a stable structure for Li ion diffusion. Mats with higher Sn content (1:3 Fe:Sn ratio) showed higher specific capacity at current densities of 100 and 200 mA g<sup>-1</sup>, but poorer performance at high current densities. Considering the current need for flexible, free-standing electrodes with stable high capacities at high current densities, and the relative simplicity of the fabrication process demonstrated here, these nanocomposite electrodes have significant potential for practical use in LIB applications.

#### Acknowledgements

This research was supported by Global Frontier Program through the Global Frontier Hybrid Interface Materials (GFHIM) of the National Research Foundation of Korea (NRF) funded by the Ministry of Science, ICT and Future Planning (2013M3A6B1078879). This research was also supported by the Technology Development Program to Solve Climate Changes of NRF-2016M1A2A2936760. S.S. Yoon expresses his appreciation to the Vice Deanship of Scientific Research Chairs at King Saud University for the partial support to this work.

#### Appendix A. Supplementary data

Supplementary data related to this article can be found at <http://dx.doi.org/10.1016/j.jallcom.2017.01.057>.

#### References

- [1] P. Lian, S. Liang, X. Zhu, W. Yang, H. Wang, *Electrochim. Acta* 58 (2011) 81–88.
- [2] G. Xia, N. Li, D. Li, R. Liu, C. Wang, Q. Li, X. Lü, J.S. Spindelw, J. Zhang, G. Wu, *ACS Appl. Mater. Interfaces* 5 (2013) 8607–8614.
- [3] R. Liu, W. Su, P. He, C. Shen, C. Zhang, F. Su, C.-A. Wang, *J. Alloys Compd.* 688 (2016) 908–913.
- [4] S. Liu, R. Wang, M. Liu, J. Luo, X. Jin, J. Sun, L. Gao, *J. Mater. Chem. A* 2 (2014) 4598.
- [5] D. Fang, L. Li, W. Xu, G. Li, Z. Luo, Y. Zhou, J. Xu, C. Xiong, *Mater. Res. Express* 1 (2014) 025012.
- [6] M.M. Rahman, A.M. Glushenkov, T. Ramireddy, T. Tao, Y. Chen, *Nanoscale* 5 (2013) 4910–4916.
- [7] F. Mueller, D. Bresser, V.S.K. Chakravadhanula, S. Passerini, *J. Power Sources* 299 (2015) 398–402.
- [8] W. Zhou, C. Cheng, J. Liu, Y.Y. Tay, J. Jiang, X. Jia, J. Zhang, H. Gong, H.H. Hng, T. Yu, H.J. Fan, *Adv. Funct. Mater.* 21 (2011) 2439–2445.
- [9] Y. Yan, F. Du, X. Shen, Z. Ji, H. Zhou, G. Zhu, *Dalton Trans.* 43 (2014) 17544–17550.
- [10] S.A. Palaparty, R.L. Patel, X. Liang, *RSC Adv.* 6 (2016) 24340–24348.
- [11] Y. Wang, H. Zhang, R. Hu, J. Liu, T. van Ree, H. Wang, L. Yang, M. Zhu, *J. Alloys Compd.* 693 (2017) 1174–1179.
- [12] W. Xie, S. Li, S. Wang, S. Xue, Z. Liu, X. Jiang, D. He, *ACS Appl. Mater. Interfaces* 6 (2014) 20334–20339.
- [13] J. Guo, L. Chen, G. Wang, X. Zhang, F. Li, *J. Power Sources* 246 (2014) 862–867.
- [14] Z. Wang, W. Zhang, X. Li, L. Gao, *J. Mater. Res.* 31 (2016) 1648–1664.
- [15] S. An, B.N. Joshi, M.W. Lee, N.Y. Kim, S.S. Yoon, *Appl. Surf. Sci.* 294 (2014) 24–28.
- [16] D.-H. Nam, J.W. Kim, J.-H. Lee, S.-Y. Lee, S.-H. Lee, Y.-C. Joo, *J. Mater. Chem. A* 3 (2015) 11021–11030.
- [17] A.L. Yarin, B. Pourdeyimi, S. Ramakrishna, *Fundamentals and Applications of Micro-and Nanofibers*, Cambridge University Press, 2014.
- [18] L. Ji, O. Toprakci, M. Alcoutlabi, Y. Yao, Y. Li, S. Zhang, B. Guo, Z. Lin, X. Zhang, *ACS Appl. Mater. Interfaces* 4 (2012) 2672–2679.
- [19] X. Han, Y. Liu, Z. Jia, Y.-C. Chen, J. Wan, N. Weadock, K.J. Gaskell, T. Li, L. Hu, *Nano Lett.* 14 (2014) 139–147.
- [20] X. Chai, C. Shi, E. Liu, J. Li, N. Zhao, C. He, *Appl. Surf. Sci.* 361 (2016) 1–10.
- [21] H. Köse, A.O. Aydin, H. Akbulut, *Int. J. Hydrogen Energy* 39 (2014) 21435–21446.
- [22] N. Du, Y. Chen, C. Zhai, H. Zhang, D. Yang, *Nanoscale* 5 (2013) 4744–4750.
- [23] J. Zhu, Z. Lu, M.O. Oo, H.H. Hng, J. Ma, H. Zhang, Q. Yan, *J. Mater. Chem.* 21 (2011) 12770.
- [24] Y. Wu, M.V. Reddy, B.V. Chowdari, S. Ramakrishna, *ACS Appl. Mater. Interfaces* 5 (2013) 12175–12184.
- [25] W. Wu, Y. Zhao, J. Li, C. Wu, L. Guan, *J. Energy Chem.* 23 (2014) 376–382.
- [26] B. Zhao, Y.-T. Xu, S.-Y. Huang, K. Zhang, M.M. Yuen, J.-B. Xu, X.-Z. Fu, R. Sun, C.-P. Wong, *Electrochim. Acta* 202 (2016) 186–196.
- [27] F. Lin, H. Wang, *J. Mater. Res.* 30 (2015) 2736–2746.